

Magnetohydrodynamical Non-radiative Accretion Flows in Two-Dimensions

James M. Stone^{1*} and James E. Pringle^{2†}

¹ *Department of Astronomy, University of Maryland, College Park, MD 20742-2421 USA*

² *Institute of Astronomy, Cambridge University, Madingley Road, Cambridge CB3 0HA, UK*

1 November 2018

ABSTRACT

We present the results of axisymmetric, time-dependent magnetohydrodynamic simulations of accretion flows around black holes. The calculations begin from a rotationally supported thick torus which contains a weak poloidal field. Accretion is produced by growth and saturation of the magnetorotational instability (MRI) provided the wavelength of the fastest growing mode is less than the thickness of the torus. Using a computational grid that spans more than two decades in radius, we compare the time-averaged properties of the flow to previous hydrodynamical simulations. The net mass accretion rate is small compared to the mass inflow and outflow rates at large radii associated with turbulent eddies. Turbulence is driven by the MRI rather than convection. The two-dimensional structure of the time-averaged flow is significantly different compared to the hydrodynamical case. We discuss the limitations imposed on our results by the assumption of axisymmetry and the relatively small radial domain.

Key words: accretion: accretion discs – black hole physics – magnetohydrodynamics

1 INTRODUCTION

Low-luminosity accretion flows onto compact objects are generally thought to be non-radiative, i.e. they cannot lose internal energy through radiative cooling. The structure of such flows is a subject of great interest, and has been studied both through self-similar solutions assuming steady-state (e.g. Narayan & Yi 1994; 1995 and references therein; Abramowicz et al. 1995; Blandford & Begelman 1999) and more recently, through direct numerical hydrodynamical simulations (Igumenshchev & Abramowicz 1999, hereafter IA99; Stone, Pringle, & Begelman 1999, hereafter SPB; Igumenshchev & Abramowicz 2000).

Numerical solutions to the hydrodynamic equations offer a new opportunity to study the multidimensional and time-dependent nature of non-radiative accretion flows. In a purely hydrodynamical flow accretion must be driven by the addition of an anomalous shear stress to the equations of motion. The form and amplitude of this stress is arbitrary; often it is assumed to take the form of a kinematic viscosity with coefficient $\nu = \alpha C_s^2 / \Omega$, where α is a dimensionless constant, C_s the sound speed, and Ω the orbital frequency (Shakura & Sunyaev 1973). Despite this limitation, the simulations reveal a variety of interesting characteristics

of such flows. For example, SPB found that, regardless of the amplitude of the anomalous shear stress, the flow at small radii is dominated by strong radial convective motions. The mass flux associated with the convective eddies is very large compared to the net mass accretion rate through the disks, which is determined by the properties of the accretion flow at the inner boundary. For small values of the anomalous shear stress, these results were in good agreement with earlier work by IA99. However, for very large shear stresses, IA99 found that convection could be suppressed, and a more laminar inflow/outflow solution was possible. These differences appear to be sensitive to the details of the assumed anomalous stress (Miller & Stone 2000). In particular, if all components of the viscous stress tensor are included in the equations of motion (so that the stress represents a true kinematic viscosity), then convection is suppressed at large values of α since the Reynolds number of the flow is then very small. On the other hand, if only the azimuthal components of the stress are included (in order to represent the highly anisotropic nature of the shear stress generated by magnetohydrodynamic turbulence, see Balbus & Hawley 1998), then strongly buoyant convective bubbles are observed even at large values of the shear stress.

The vanishingly small accretion rates observed at small α in both IA99 and SPB have been interpreted as due to inward angular momentum transport in axisymmetric convective flows. Recently, self-similar solutions which re-

* E-mail: jstone@astro.umd.edu

† E-mail: jep@ast.cam.ac.uk

produce the properties of the simulations have been described by Narayan, Abramowicz, & Igumenshchev (2000) and Quataert & Gruzinov (2000). These authors argue that in three-dimensions (3D), turbulent mixing of convective eddies might transport angular momentum outwards, and so change the qualitative nature of the flow (although 3D direct numerical simulations of turbulent convection in *thin* accretion disks have shown that in this case, angular momentum is not carried outwards: Stone & Balbus 1996; Cabot 1996). Fortunately, fully 3D simulations of hydrodynamical non-radiative accretion flows that test these ideas are possible (Igumenshchev, Abramowicz, & Narayan 2000; Miller & Stone 2000); it is found that in 3D the flows are qualitatively and quantitatively similar to the axisymmetric models, and moreover, that angular momentum transport in thick disks via radial convection is vanishingly small, or perhaps even inward. A kinetic theory for hydrodynamic turbulence in accretion flows that can account for these results has been developed by Quataert & Chiang (2000). A low mass accretion rate and central density is one possible interpretation of the low flux of high-energy emission observed from black holes at the center of early-type galaxies (Di Matteo, Carilli, & Fabian 2000), and the possible detection of polarized emission from the galactic center (Agol 2000; Quataert & Gruzinov 2000).

While understanding the properties of hydrodynamical accretion flows driven by an anomalous shear stress is important, it is generally agreed that angular momentum transport is in fact mediated by magnetic stresses, either through magnetohydrodynamic (MHD) turbulence driven by the magnetorotational instability (MRI) (Balbus & Hawley 1998), or global stresses associated with a magnetocentrifugal wind (Blandford & Payne 1981). Thus, it is essential to extend the hydrodynamical models to MHD. In this paper we present the results of a series of MHD simulations of non-radiative accretion flows in which accretion is driven self-consistently by magnetic stresses within the flow.

The evolution of magnetized accretion flows has been studied via numerical methods in a variety of contexts. Studies of thin disks threaded by a vertical field have been reported by a number of authors (Shibata & Uchida 1986; Stone & Norman 1994; Matsumoto et al. 1996; Kudoh et al. 1998). Rapid collapse of the disk is observed in these calculations, driven either by axisymmetric modes of the MRI when the field is weak, or by magnetic braking effects when the field is strong. On the other hand, the nonlinear stage of the MRI has been studied extensively in local 3D simulations (Hawley, Gammie, & Balbus 1995; 1996 hereafter HGB; Brandenburg et al. 1995; Stone et al. 1996), and more recently global 3D simulations (Matsumoto 1999; Armitage 1998; Hawley 2000). In this case, MHD turbulence is the inevitable outcome of the MRI.

The study of Hawley (2000) in particular is relevant to the results presented here. He presents a number of time-dependent MHD simulations of accretion onto a black hole in two- and three-dimensions, beginning from a pressure supported torus with a weak, embedded magnetic field. In each case, development of the MRI produces MHD turbulence and accretion after only a few orbits. Comparison of the evolution of axisymmetric and fully 3D simulations reveals important differences. In 3D development of the non-axisymmetric MRI increases the level of MHD turbulence

and sustains mass accretion throughout the entire evolution, whereas in the axisymmetric models accretion dies away on long timescales as there is no dynamo action to maintain poloidal field.

The results presented in this paper are in many ways complementary to those of Hawley (2000). Although we limit this study entirely to axisymmetric models, this allows us to afford a much larger radial domain than current 3D models (more than a factor of ten in some cases). This introduces a very large range of dynamical timescales between the inner and outer regions of the disk. Thus, although turbulence and accretion inevitably die away in axisymmetry after a few orbits of the outer disk, the inner disk undergoes thousands of orbits in this same period. Thus, the flow may reach a quasi steady-state in the inner regions, which can be compared and contrasted to the steady-state structure found for purely hydrodynamical models. In fact, we find both important differences and similarities between axisymmetric hydrodynamical models (e.g. SPB) and the MHD models described here. For example, convective instabilities appear to play little role in determining the two-dimensional structure of the flow, instead turbulence driven by the MRI dominates. We find that unbound outflows can be produced by magnetic stresses in models with strong poloidal fields. In every case we have studied here, the mass accretion rate is once again small (compared to the expectations of some self-similar steady-state solutions such as Advection Dominated Accretions Flows or ADAFs; Narayan & Yi 1995), and determined by the flow properties at the inner boundary. It will, however, be important to test these results with three-dimensional simulations that span a large radial domain.

The paper is organized as follows. In §2 we describe our methods, in §3 we present our results, in §4 we discuss these results, and in §5 we summarize and conclude.

2 METHOD

2.1 The Equations of Motion

To compute the models discussed here, we solve the equations of MHD

$$\frac{d\rho}{dt} + \rho \nabla \cdot \mathbf{v} = 0, \quad (1)$$

$$\rho \frac{d\mathbf{v}}{dt} = -\nabla P - \rho \nabla \Phi + \frac{1}{4\pi} (\nabla \times \mathbf{B}) \times \mathbf{B} \quad (2)$$

$$\rho \frac{d(e/\rho)}{dt} = -P \nabla \cdot \mathbf{v} + \eta \mathbf{J}^2 \quad (3)$$

$$\frac{\partial \mathbf{B}}{\partial t} = \nabla \times (\mathbf{v} \times \mathbf{B} - \eta \mathbf{J}) \quad (4)$$

where ρ is the mass density, P the pressure, \mathbf{v} the velocity, e the internal energy density, \mathbf{B} the magnetic field, and $\mathbf{J} = (c/4\pi) \nabla \times \mathbf{B}$ the current density. Note that the equations of motion do not contain any anomalous shear or viscous stress terms. We adopt an adiabatic equation of state $P = (\gamma - 1)e$, and consider models with $\gamma = 5/3$. These equations are solved in spherical polar coordinates (r, θ, ϕ) .

The final terms in equations [3] and [4] are the magnetic heating and diffusion rates mediated by a finite resistivity η . For numerical schemes that solve the internal (rather than

total) energy equation [3], numerical diffusion of the magnetic field can result in the loss of energy from the system. We expect this effect could be important for the adiabatic and turbulent flows studied here. In order to capture this energy in the form of heating at current sheets, we have added an anomalous resistivity of the form

$$\eta = \eta_0 |\mathbf{J}| \quad (5)$$

The form for η_0 and the implementation in our numerical code is described in an Appendix. Comparison of the evolution of magnetized tori with and without an anomalous resistivity show that in the former case total energy conservation is improved to better than one part in a thousand. Note that by making the anomalous resistivity proportional to the current density, we ensure it is large in current sheets (and therefore spreads them out over enough zones to be resolved), but has negligible effect in smooth regions of the flow. Thus, the anomalous resistivity adopted here plays a role analogous to the artificial viscosity used to capture shocks (Stone & Norman 1992a).

All of the simulations presented here use the pseudo-Newtonian gravitational potential introduced by Paczyński & Wiita (1980)

$$\Phi = -\frac{GM}{r - R_G} \quad (6)$$

to approximate general relativistic effects in the inner regions. In particular, this potential reproduces the last stable circular orbit at $r = 3R_G$. Thus, the flows we study here are primarily intended to model accretion onto a non-rotating black hole. We find the use of this potential simplifies the inner boundary condition for the magnetic field, as discussed below.

2.2 Initial Conditions

As in SPB, our simulations begin with an exact equilibrium state consisting of a constant angular momentum torus embedded in a non-rotating, low-density ambient medium in hydrostatic equilibrium. The pressure, density, and angular velocity in the torus initially are given by an analytic solution generated by the procedure described by Papaloizou & Pringle (1984), see SPB for details. The shape and size of the torus are controlled by two parameters, the distortion parameter d and the maximum density ρ_{max} , as well as the polytropic index $n = (\gamma - 1)^{-1}$. We adopt $d = 1.5$ and $\rho_{max} = 1$ for all the models computed here. Note we use a larger value of d than the models presented in SPB; this gives a thicker torus initially in which there is a larger dynamic range of unstable modes for the MRI. The torus is embedded in an ambient medium with constant density $\rho_0 = 10^{-4}$ and pressure $P_0 = \rho_0/r$.

The magnetic field which threads the torus initially is generated by a vector potential, i.e. $\mathbf{B} = \nabla \times \mathbf{A}$. Initializing the field in this way guarantees it will be divergence free. We take \mathbf{A} to be purely azimuthal with

$$A_\phi = \rho^2 / \beta_0 \quad (7)$$

where β_0 is an input parameter that specifies the magnetic field strength. This form for \mathbf{A} generates poloidal field loops that are parallel to the density contours, and with an amplitude such that the parameter β_0 corresponds approximately

to the plasma β -parameter (where $\beta \equiv 8\pi P/B^2$) in the interior of the torus initially. Note that in contrast to some earlier studies of the evolution of magnetized accretion disks (e.g. Shibata & Uchida 1986; Stone & Norman 1994), the magnetic field is initially confined to the interior of the torus and does not connect to the ambient medium.

2.3 Numerical Methods

All of the calculations presented here use the ZEUS-2D code described by Stone & Norman (1992a; 1992b). Several minor modifications to the code were required for the calculations presented here, including implementing the Paczyński & Wiita potential, and adding the anomalous resistivity as described in the Appendix.

The pseudo-Newtonian potential introduces a radial scale into the problem: the radius of the event horizon R_G . Our computational grid extends from an inner boundary at $r = 2R_G$ to either $160R_G$ (with the density maximum of the torus located initially at $R_0 = 40R_G$), or $400R_G$ (with $R_0 = 100R_G$). In the latter case, this gives a spatial dynamic range over which an accretion flow can be established of nearly two orders of magnitude. This range is smaller than that used by SPB because of the much greater computational cost of MHD compared to hydrodynamical simulations, primarily caused by the much smaller timestep enforced by stability requirements in regions of high Alfvén speed. Some models have been evolved for up to 5 million cycles, taking more than 400 hours on a modern workstation.

As in SPB, we adopt a non-uniform, logarithmically spaced grid, so that $(\Delta r)_{i+1}/(\Delta r)_i = N_r^{-1}\sqrt{10}$. This gives a grid in which $\Delta r \propto r$, with N_r grid points per decade in radius. Similarly, we adopt non-uniform angular zones with $(\Delta\theta)_j/(\Delta\theta)_{j+1} = N_\theta^{-1}\sqrt{4}$ for $0 \leq \theta \leq \pi/2$ (that is the zone spacing is decreasing in this region), and $(\Delta\theta)_{j+1}/(\Delta\theta)_j = N_\theta^{-1}\sqrt{4}$ for $\pi/2 \leq \theta \leq \pi$. This gives a refinement by a factor of four in the angular grid zones between the poles and equator. Equatorial symmetry is not assumed. Our standard resolution is $N_r = 64$ and $N_\theta = 44$. We have also computed a high resolution model with $N_r = 128$ and $N_\theta = 80$.

We adopt outflow boundary conditions (projection of all dynamical variables except the magnetic field) at both the inner and outer radial boundaries. For the magnetic field at the outer radial boundary we use an outflow condition (projection of each component), whereas at the inner boundary we use a negative-stress condition (that is we enforce $B_r B_\phi \leq 0$ at $r = 2R_G$). This ensures there is no outward flux of energy or angular momentum at the inner boundary. Our radial grid is large enough that the outer boundary condition has little effect. Moreover, the use of the pseudo-Newtonian potential greatly simplifies the inner boundary condition provided the inner edge of the grid is well within the last stable orbit, because in this case a super-Alfvénic inflow is always present there. In the angular direction, the boundary conditions are set by symmetry at the poles.

3 RESULTS

Table 1. Properties of Simulations

Run	β_o	Resolution ^(a)	R_0/R_G	t_f (orbits ^(b))
A	100	64	40	5.08
B	200	64	40	5.82
C	400	128	40	5.41
D	∞	64	40	5.00
E	100	32	100	5.25
F	200	64	100	4.50
G	∞	64	100	4.00

(a) grid points per decade in radius, (b) at $r = R_0$

3.1 A Fiducial Model

Table 1 summarizes the properties of the simulations discussed here. Columns two through five give the initial field strength (as measured by β_o), the numerical resolution, the radial extent of the numerical grid expressed as the ratio R_0/R_G , and the final time t_f at which each simulation is stopped (all times in this paper are reported in units of the orbital time at $r = R_0$).

Run C has the highest resolution and weakest initial magnetic field, and therefore the largest range in unstable wavelengths of the MRI: we discuss it first (we find the fastest growing mode of the MRI is unresolved in this case at lower resolution, see below). Figure 1 plots the time evolution of the density in Run C. In each panel, gray shading is used to denote regions of the torus in which $v_r > 0$. The growth rate of the MRI is highest near the inner edge of the torus (since the angular frequency Ω is largest there), thus saturation of the MRI produces inward mass flow from the inner edge of the torus first. In local axisymmetric simulations of the MRI with initially uniform vertical fields (Hawley & Balbus 1992), an organized flow consisting of two oppositely directed radial streams called the channel solution emerges in the nonlinear regime. There is no evidence that the channel solution persists over a large range of radii in these global models; such solutions are found to dominate axisymmetric simulations of thin disks (e.g. Stone & Norman 1994). This may be a result of the radial variation in density and magnetic field within the torus, or because of the rapid change in timescales with radius, so that channels that form first at the inner edge quickly encounter slower material as they move outwards. Accretion through the inner boundary begins between 1 and 2 orbits. Thereafter, the accretion flow thickens considerably. Wiggles in the contours indicate the presence of large amplitude density fluctuations, and moreover the complex pattern of shading indicates both inward and outward moving fluid elements are located at all angles. Overall, the flow has many similarities to the hydrodynamical torus (see Figure 1 of SPB), although in this case the fluctuations in the flow are not driven by convection but rather the MRI.

The effect of numerical resolution on the nonlinear stage of the MRI has been examined in a variety of local studies (e.g. HGB). If the fastest growing mode is unresolved, saturation of the instability occurs later and at a lower amplitude for the magnetic energy. Detailed analysis of the initial conditions in Run C show that over most of the central regions of the torus $\lambda_c/\Delta x \approx 6$, where λ_c is the wavelength of the

fastest growing mode of the MRI given by $\lambda_c = 2\pi V_A/\sqrt{3}\Omega$ (V_A and Ω are the Alfvén speed and orbital frequency respectively), and Δx is the grid size. This indicates Run C is resolved, but just barely so. Indeed, if Run C is repeated at a lower resolution, collapse of the torus is delayed, and fluctuations of, e.g. the density, are reduced. Due to the increase in the grid size with radius, and variations in the Alfvén speed in the torus, there are regions where the MRI is unresolved in Run C. In order to capture the evolution and interaction of many scales within the torus, it will be important to increase the numerical resolution in future studies beyond what is possible here.

Figure 2 is a plot of the time-history of the angle-integrated mass accretion rate \dot{M}_{acc} through the inner boundary in runs with different initial field strengths, where

$$\dot{M}_{\text{acc}}(r) = 2\pi r^2 \int_0^\pi \rho v_r \sin \theta d\theta. \quad (8)$$

The data has been binned over 0.03 orbit intervals to construct the plot, the instantaneous mass accretion rate shows even more rapid fluctuations than are evident in Figure 2. It is clear that at early times, the mass accretion rate depends on the field strength: not surprisingly stronger fields have higher \dot{M}_{acc} . Only Run B ($\beta_o = 200$) appears to reach a quasi-steady state; in Run A ($\beta_o = 100$) the accretion rate is highly variable, while in Run C (the fiducial model, $\beta_o = 400$) it shows a slow but steady decline (although it seems to flatten out beyond orbit 4). This decline is likely related to the anti-dynamo theorem for axisymmetric flows; we discuss the differences between these models in more detail in §3.2. Note that each orbit at $r = R_0$ corresponds to nearly one hundred orbits at the inner boundary, thus the decline in \dot{M}_{acc} in Run C occurs over many dynamical times for the inner regions of the flow. Shown as a dotted line in Figure 2 is the mass accretion rate for a purely hydrodynamical model computed using the Paczyński & Wiita potential, an anomalous shear stress of the form $\nu = 10^{-2}\rho$ (see SPB), and a grid identical to that used for Runs A and B (hereafter we refer to this model as Run D). It shows a remarkably similar profile to Run A, indicating that the magnetic stresses responsible for accretion must have approximately the same amplitude as this hydrodynamical model. That is, the mass accretion rate in these MHD models is small compared to what might be expected in an ADAF, just as in the hydrodynamical models of SPB.

Figure 3 plots the instantaneous structure of a number of quantities in the inner regions $r < 20R_G$ of Run C at $t = 3.25$ orbits. The flow is clearly complex (and is also

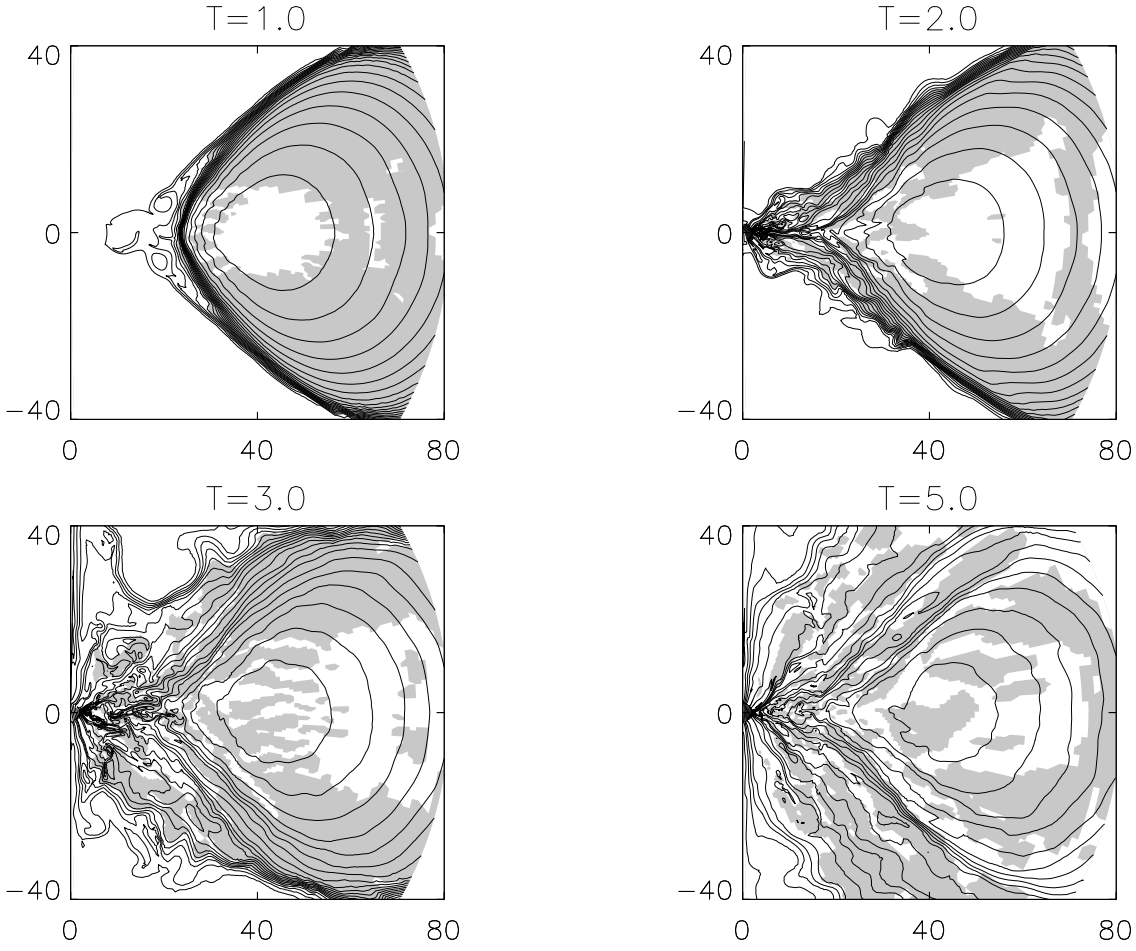


Figure 1. Evolution of the density in a fiducial model (Run C). Time is measured in units of the orbital time at $r = 40R_G$. The axes are labeled in units of R_G . Twenty logarithmic contours are used between the density maximum (0.97, 0.96, 0.94, and 0.85 for $t = 1, 2, 3$ and 5 orbits respectively) and 10^{-4} . The shaded regions have $v_r > 0$.

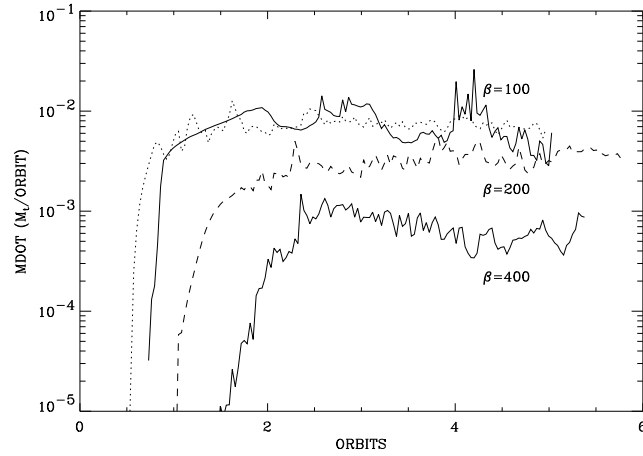


Figure 2. Total mass accretion rate through the inner boundary for models with different initial magnetic field strengths. The solid and dashed lines labeled $\beta = 100$, $\beta = 200$, and $\beta = 400$ correspond to models A, B, and C (the fiducial model) respectively. The dotted line shows the mass accretion rate for a purely hydrodynamical model (Run D) with an anomalous shear stress $\nu = 10^{-2}\rho$.

highly time-dependent). Within $3R_G$ the profiles of each variable become radial as the gas free-falls inward. However, beyond this region each variable is dominated by large amplitude fluctuations. There is some anti-correlation between the density and entropy fluctuation, although not as much as in the purely hydrodynamical case (SPB). This is an indication that the velocity field which gives rise to the density fluctuations is not driven by entropy gradients, i.e. that convection is not as important in these MHD models (see also below). That the entropy gradients do not drive the flow in these simulations is also demonstrated by setting the anomalous resistive heating rate to zero. In this case, we find turbulence and accretion continue despite the lack of heating associated with dissipation of the magnetic field.

The magnetic pressure associated with the azimuthal component of the field is largest above and below the midplane of the flow (and is in fact near zero in many regions close to the midplane), which may be an indication of the effect of magnetic buoyancy, or enhanced dissipation in regions of large current density. The $r - \phi$ component of the Maxwell stress is highly disordered in regions of the highest density (within 30° of the midplane). This result is consistent with the saturated stage of the axisymmetric modes of the MRI in fields with no net flux (Hawley & Balbus 1992).

In Figure 4 we plot two-dimensional contours of a large number of quantities in Run C averaged between orbits 2.5 and 4.6. Only 42 data files have been used to construct this plot, thus many of the contours are noisy. Nonetheless, several important trends can be identified, especially in comparison to the hydrodynamical case (Figure 4 of SPB). Firstly, the contours of density and pressure are much more similar in Run C than in the hydrodynamical models. As a result, the contours of the entropy S are no longer nearly parallel to the contours of the specific angular momentum $l = v_\phi r \sin \theta$, instead the latter are more nearly parallel to cylindrical radii than the former. In a purely hydrodynamical flow convection was found to be efficient enough to keep the contours of S and l nearly parallel. In the MHD flow the contours of the angular frequency Ω are nearly parallel to cylinders, whereas in the hydrodynamical case they were more spherical. It would appear that one action of the magnetic field is to try to reduce the vertical gradients of Ω . In SPB it was argued that the ordering of variables based on the shape of their contours was consistent with marginal stability to the Høiland criterion (Begelman & Meier 1982; Blandford & Begelman 1999). However, this ordering does not apply to the MHD flow shown in Figure 4, confirming that even a weak magnetic field changes the fundamental stability properties of a rotating and stratified flow (Balbus 1995).

Also plotted over the contours of Ω in Figure 4 are vectors showing the direction of the poloidal magnetic field at $t = 3$ orbits. The length of each vector has been scaled to unity, so that they indicate the direction but not the magnitude of the field. The vectors reveal a highly tangled pattern in a wedge within 45° of the equator, consistent with the expected geometry of the field in MHD turbulence. Towards the poles the field becomes much more ordered. We use a snapshot to show the field geometry rather than a time average because within the disk the fluctuating field averages nearly to zero.

3.2 Effect of variation of field strength

In order to investigate the effect of the initial magnetic field strength on the nature of the resulting accretion flow, we have calculated two models identical to the fiducial model but with $\beta_o = 100$ and 200 respectively; these are labeled Runs A and B in Table 1. We have also calculated models with the same initial magnetic field strength as Runs A and B, but which extend over a radial domain which is 2.5 times larger than the fiducial model; these are labeled Runs E and F in Table 1.

The range of initial magnetic field strengths that can be studied in the present set of experiments is limited by the numerical resolution (which sets a lower limit) and the size of the torus (which sets an upper limit). Fields with $\beta_o < 100$ initially are too strong for λ_c to be smaller than the thickness of the torus, we do not present results from such models here. For models with $100 < \beta_o < 400$ global stresses from the radial component of the field loops inside the torus produces magnetic stresses, outward angular momentum transport, and inward accretion before the MRI becomes nonlinear. This is especially evident in Runs A and E, where accretion begins after only about 0.7 orbits. The accretion flow driven by global stresses associated with a smooth field is very different from the complex flow associated with accretion driven by the saturated MRI. Figure 5 plots two-dimensional contours of a variety of quantities in Run F averaged over orbits 2 through 3 using 20 data files. Comparison of Figures 4 and 5 reveal many differences. The accretion flow in Run F is confined to a thin, dense, wedge near the equatorial plane. A strong and smooth toroidal field is located above and below the midplane, strong vertical gradients in B_ϕ^2 compress the wedge. Perhaps the only similarity between Figures 5 and 4 is that once again contours of Ω are parallel to cylinders. Contours of the specific angular momentum show that the material slightly above the midplane has a higher l than material at the midplane (in the dense wedge there). This is evident as a small, outward bump in the contours of l at the midplane.

A snapshot of the direction of the magnetic field (but not its magnitude) in Run F at $t = 2$ orbits is shown by arrows plotted over the contours of Ω in Figure 5. Note that in contrast to the pattern of the field lines in Run C (shown in Figure 4), at early times in Run F the field is largely ordered throughout the flow. Close to the dense disk at the equatorial plane the field lines are highly inclined to the vertical, but become more radial towards the poles.

The contours of l in Figure 5 indicate that magnetic stresses associated with an ordered poloidal magnetic field have resulted in a deficit of angular momentum in material at the midplane, and an excess of angular momentum in the material above it. For this reason, material above the midplane flows outward in a magnetocentrifugal outflow (e.g., Blandford & Payne 1981). A small fraction of this outflow near the poles is strongly unbound (with total energy $E > 0$), however most of the denser outflow within 45° of the midplane is still bound. The ratio of the mass outflow to accretion rate at the midplane is 0.1 at $r = 6R_G$, and increases only slightly to 0.2 by $r = 50R_G$. The flow at this time bears a striking similarity to previous two-dimensional global models of thin accretion disks (Shibata & Uchida 1986; Stone & Norman 1994) threaded by a strong verti-

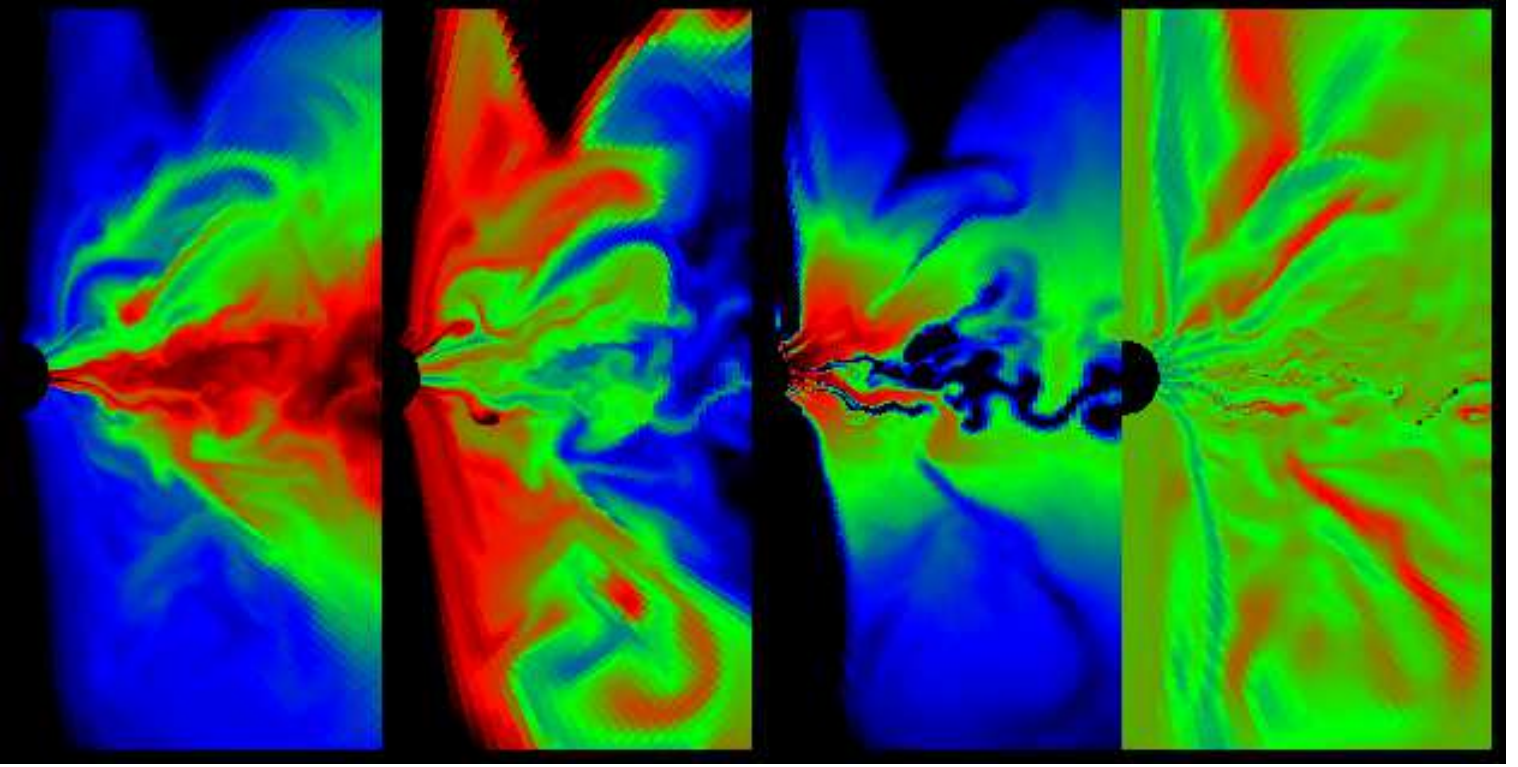


Figure 3. (from left to right) Images of the logarithm of the density, specific entropy, B_ϕ^2 , and $r - \phi$ component of the Maxwell stress normalized by the magnetic pressure, i.e. $2B_r B_\phi / B^2$, at $t = 3.25$ orbits in the inner region $r < 20R_G$ of Run C. The colour table runs from black to blue through red to black. The minimum and maximum of $\log \rho$ are -3.5 and -0.6, of S are -1 and 2, of B_ϕ^2 are 0 and 3, and of $2B_r B_\phi / B^2$ are -1.6 and 2.8.

cal magnetic field. Accretion and outflow in these thin disk simulations was driven (for strong fields) by magnetic braking due to the effects of a nonrotating corona in which the disk was embedded whereas in Run F, the global stresses which drive accretion and outflow are associated with a radial magnetic field that connects the inner and outer regions of the torus.

Inevitably, growth and saturation of the MRI in the denser regions of the torus, where the radial field is initially smaller, perturbs and eventually overwhelms the smooth accretion flow shown in Figure 5. As a consequence, at late times (after orbit 3) Run F reverts to a structure similar to Figure 4, that is a turbulent and rapidly fluctuating flow driven by the MRI.

From Figure 2, it is clear that the mass accretion rate depends on the initial magnetic field strength, with Run A having the highest \dot{M}_{acc} . It is possible that even stronger vertical fields could drive a higher \dot{M}_{acc} , a more powerful outflow, and suppress the poloidal modes of the MRI. On the other hand, it is unlikely that such a configuration will be stable to the nonaxisymmetric MRI, thus 3D turbulent accretion dominated by the MRI may be a more likely outcome.

3.3 Models over a larger radial domain

Runs E through G listed in Table 1 are identical to models A, B, and D respectively, except the density maximum of the torus is located at $r = 100R_G$ initially. These mod-

els are considerably more expensive to compute, because of the larger range in dynamical times between the inner and outer regions of the grid. Thus, we have not been able to calculate the evolution of a $\beta_o = 400$ model (which requires 128 grid points per decade in radius) over this large a radial domain. Since these runs span a larger radial domain, they are the more suitable for studying the radial profiles of time-averaged variables in a MHD non-radiative accretion flow. On the other hand, because our models are axisymmetric, the flow never becomes steady over dynamical times associated with the outer regions of the disk. Since there are roughly 350 orbits of the disk near the inner boundary for every orbit at $r = R_0$ in these models, however, the flow may be quasi-steady in the inner regions.

Figure 6 plots the radial profiles of a variety of variables in Run F angle-averaged over a small wedge near the mid-plane (between $\theta = 84$ and 96 degrees), and time-averaged over 41 data files covering orbits 3 through 5. This plot can be directly compared to Figure 5 in SPB. The location of the last stable circular orbit is indicated by the vertical dotted line in each panel. Note that this same run was shown at an earlier time in Figure 5, where it was noted that accretion was dominated by global stresses rather than the MRI. However, by orbit 3 and for all times thereafter accretion of denser material driven by the nonlinear stage of the MRI dominates the flow.

In the hydrodynamical models of SPB, the profiles of each variable became simple power-laws, whereas in these MHD models the profiles are more complex. For example,

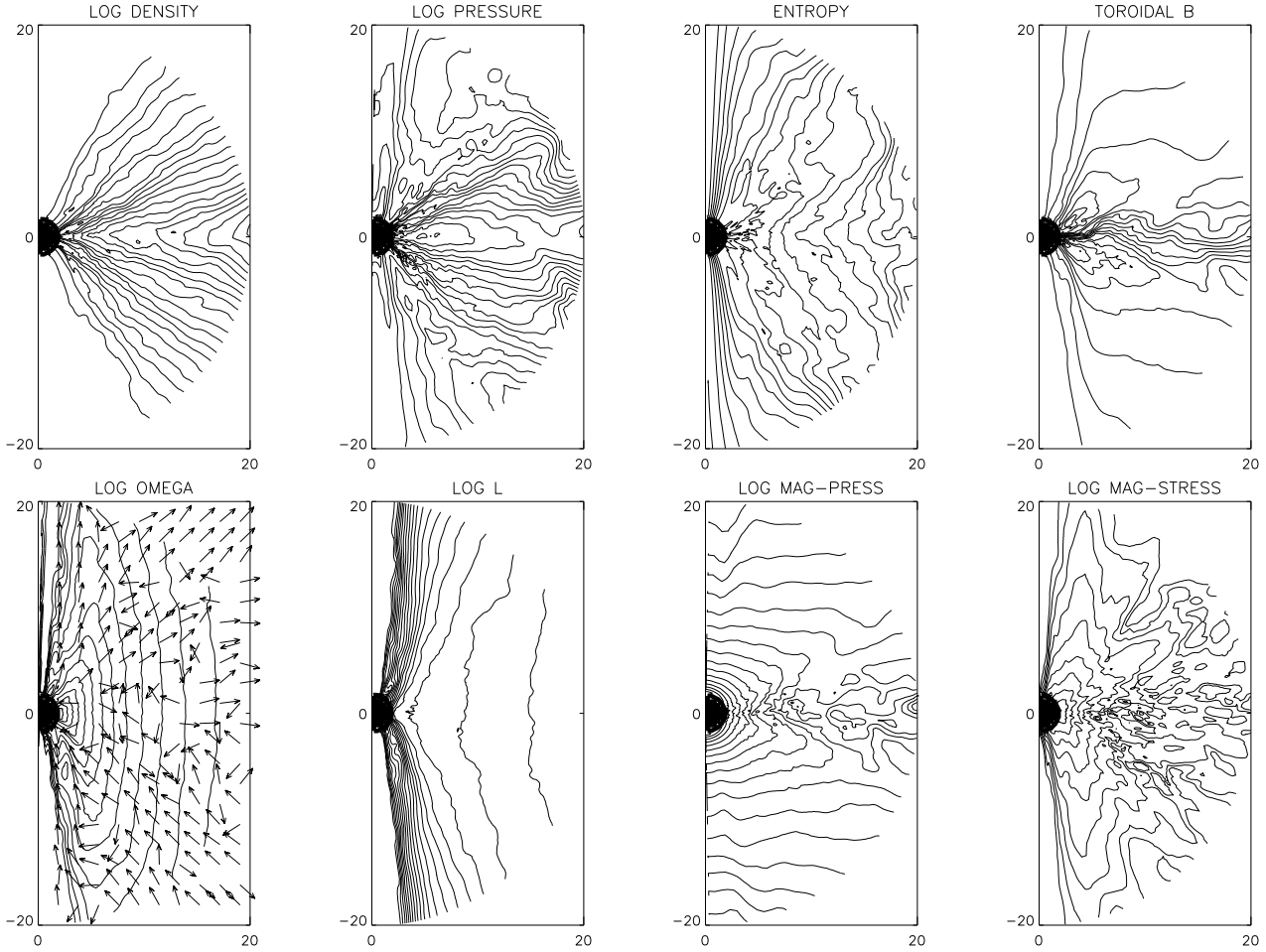


Figure 4. Two-dimensional structure of a variety of time-averaged quantities from the fiducial model (Run C). The minimum and maximum of $\log \rho$ are -3 and -0.71, of $\log P$ are -4.0 and -1.6, of S are -0.82 and 3.3, of B_ϕ are -0.19 and 0.21, of $\log \Omega$ are 0.48 and 2.1, of $\log l$ are -2 and -0.61, of $\log B^2/8\pi$ are -3 and -0.61, and of $\log B_r B_\phi/4\pi$ are -4 and -1.3. Twenty equally spaced contour levels are used, except $B_r B_\phi/4\pi$ for which ten are used. The direction of the magnetic field at $t = 3$ orbits is shown by unit vectors plotted over the contours of Ω

the density is largely constant, although it increases by a factor of about two near the outer edge. The thermal and magnetic pressures are identical at $r = 3R_G$, and both decrease rapidly beyond roughly as $r^{-3/2}$. Note that the ratio of the gas to magnetic pressure (β) is always greater than one beyond $r = 6R_G$. The rotational velocity is nearly Keplerian beyond $6R_G$, interior to this point it decreases rapidly. Interestingly, the radial velocity increases sharply for $r < 6R_G$ as well, so that at $r = 3R_G$ it is nearly equal to both the sound and Alfvén speed. Rapid infall is therefore beginning well beyond the radius of the last stable circular orbit. Beyond $6R_G$ the decline in the radial velocity is consistent with r^{-1} .

The magnetic stress, normalized to the magnetic pressure, is nearly constant beyond $6R_G$ with $\alpha_{mag} = 2B_r B_\phi/B^2 \approx 0.1$. (Note that α_{mag} is not the same as the Shakura-Sunyaev α parameter.) We measure the Reynolds stress using the difference between the angular momentum flux and mass flux times the mean angular momentum (Hawley 2000), i.e.

$$\langle \rho v_r \delta v_\phi \rangle = \langle \rho v_r v_\phi \rangle - \langle \rho v_r \rangle \langle v_\phi \rangle \quad (9)$$

This definition removes the uncertainty in the mean ra-

dial velocity needed to compute the Reynolds stress from the fluctuating velocity components alone. Plotting the Reynolds stress in this fashion shows that within $3R_G$ it grows rapidly in magnitude, however it is negative, indicating angular momentum is being advected inwards by the strong infall (note that only the magnitude of the Reynolds stress is shown in Figure 6). Beyond $3R_G$ the Reynolds stress is positive but very small.

Finally, plots of each component of the magnetic field show that the ϕ -component dominates over most of the radial domain. Within $6R_G$, however, the radial component increases rapidly, so that at $r = 3R_G$, $B_r \approx B_\phi$. This indicates the field is being ‘combed’ inwards by the rapid radial infall in this region.

Figure 6 reveals that the flow is strongly affected by the presence of the last stable circular orbit well beyond $r = 3R_G$. In addition, the large variations seen at large radii indicate the flow has not reached a steady-state there (nor do we expect it to in axisymmetry). This combination severely restricts the radial domain over which any self-similar steady-state profiles can be measured. For the moment the profiles are consistent with $\alpha_{mag} = \text{constant}$,

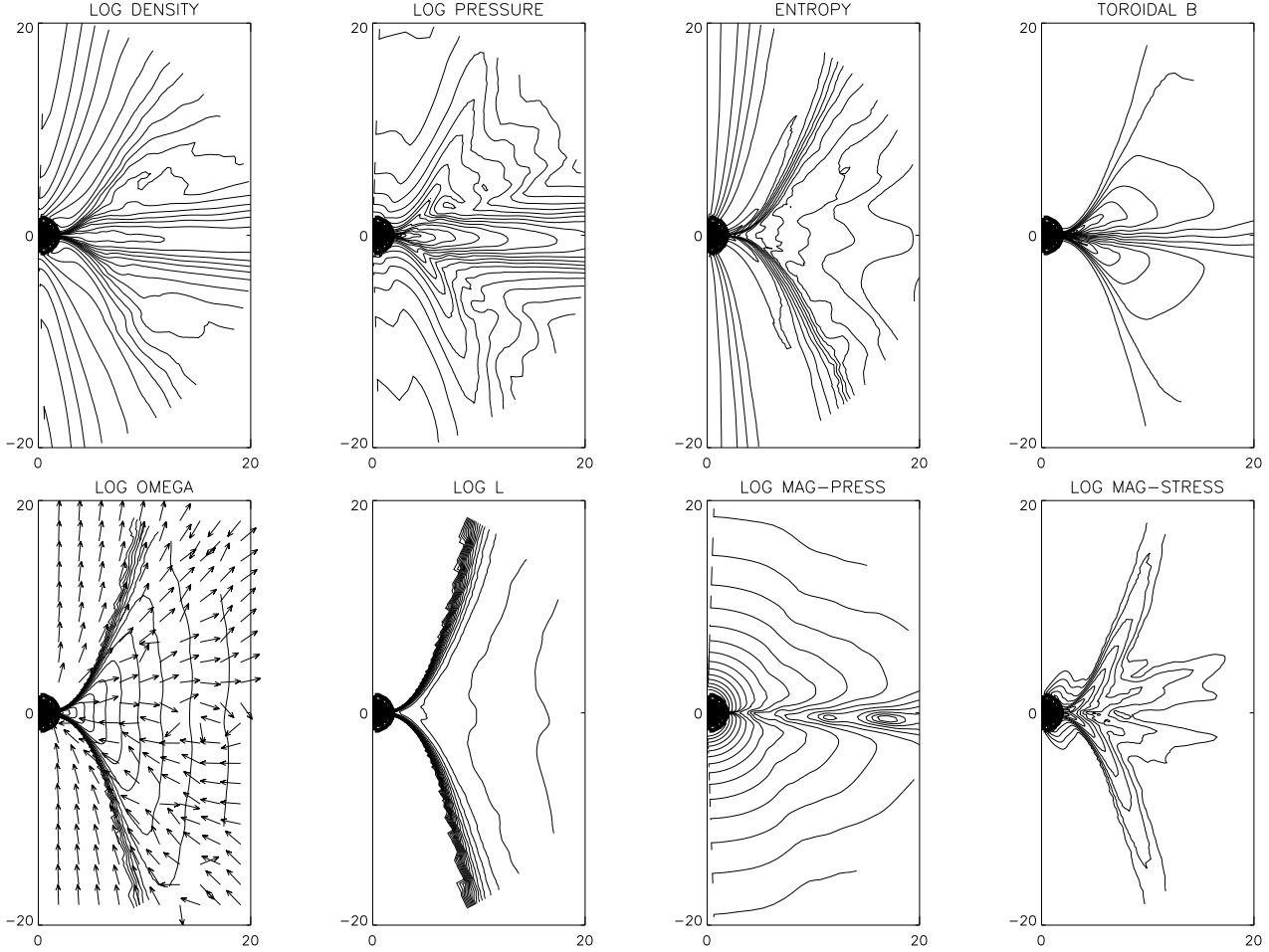


Figure 5. Two-dimensional structure of a variety of time-averaged quantities from Run F over orbits 2 through 3. The minimum and maximum of $\log \rho$ are -2.8 and -0.16, of $\log P$ are -2.9 and 0.79, of S are 0.63 and 2.3, of B_ϕ are -1.9 and 1.5, of $\log \Omega$ are 0.48 and 2.6, of $\log l$ are -2 and -0.32, of $\log B^2/8\pi$ are -1.9 and 1.6, and of $\log B_r B_\phi/4\pi$ are -2 and 0.68. Twenty equally spaced contour levels are used for each variable except $B_r B_\phi/4\pi$, for which 10 are used. The direction of the magnetic field at $t = 2$ orbits is shown by unit vectors plotted over the contours of Ω

$v_r \propto r^{-1}$, and $\rho \propto \text{constant}$. However, these profiles must be measured in a fully 3D flow that has reached a steady-state before any meaningful conclusions can be drawn from them.

The profiles of the flow within $6R_G$ are in fact of great interest in interpreting observations near the event horizon of accreting black holes. It is interesting that the large increase in the radial velocity occurs *beyond* $3R_G$, presumably because of inward pressure gradients. The inflow becomes supersonic just at $3R_G$, at which point $B_r = B_\phi$. These results are in agreement with recent models of MHD inflows near the horizon of black holes developed by Krolik (1999) and Gammie (2000), even though such models are applicable to thin disks as opposed to the thick disks studied here. We also note the magnetic stress increases sharply within $6R_G$, and is not zero at the last stable orbit. The increase in the stress results from the increase in B_r . The rapid radial infall generates an ordered radial component to the field, so that the $\langle B_r B_\phi \rangle$ correlations are strongly increased. In turn, the increased stress affects the infall. Note also from the plot of Ω in Figure 6 that $d\Omega/d \ln r$ is not zero at $3R_G$. This means the flow is not strain-free at $3R_G$, so that if the shear stress

depends on the rate-of-strain, it will not be stress-free there either.

If the nature of the flow near the inner region is set by the finite pressure gradients associated with a thick disk, as opposed to magnetic effects, similar profiles (e.g. rapid infall inside $6R_G$) should be evident in a purely hydrodynamical simulation in a pseudo-Newtonian potential. Indeed, radial profiles of v_r and C_s in Run G show a rapid increase in the infall velocity around $6R_G$, with the flow becoming supersonic at $3R_G$, despite the fact that the shear stresses in the hydrodynamical and MHD models depend on different quantities (e.g. the former depends on the rate-of-strain). Understanding the nature of the infall region and how it changes with, e.g., the disk thickness is an important problem for future studies.

By plotting the angle-integrated inward and outward mass flux rates, \dot{M}_{in} and \dot{M}_{out} respectively, defined through

$$\dot{M}_{\text{in}}(r) = 2\pi r^2 \int_0^\pi \rho \min(v_r, 0) \sin \theta d\theta \quad (10)$$

$$\dot{M}_{\text{out}}(r) = 2\pi r^2 \int_0^\pi \rho \max(v_r, 0) \sin \theta d\theta \quad (11)$$

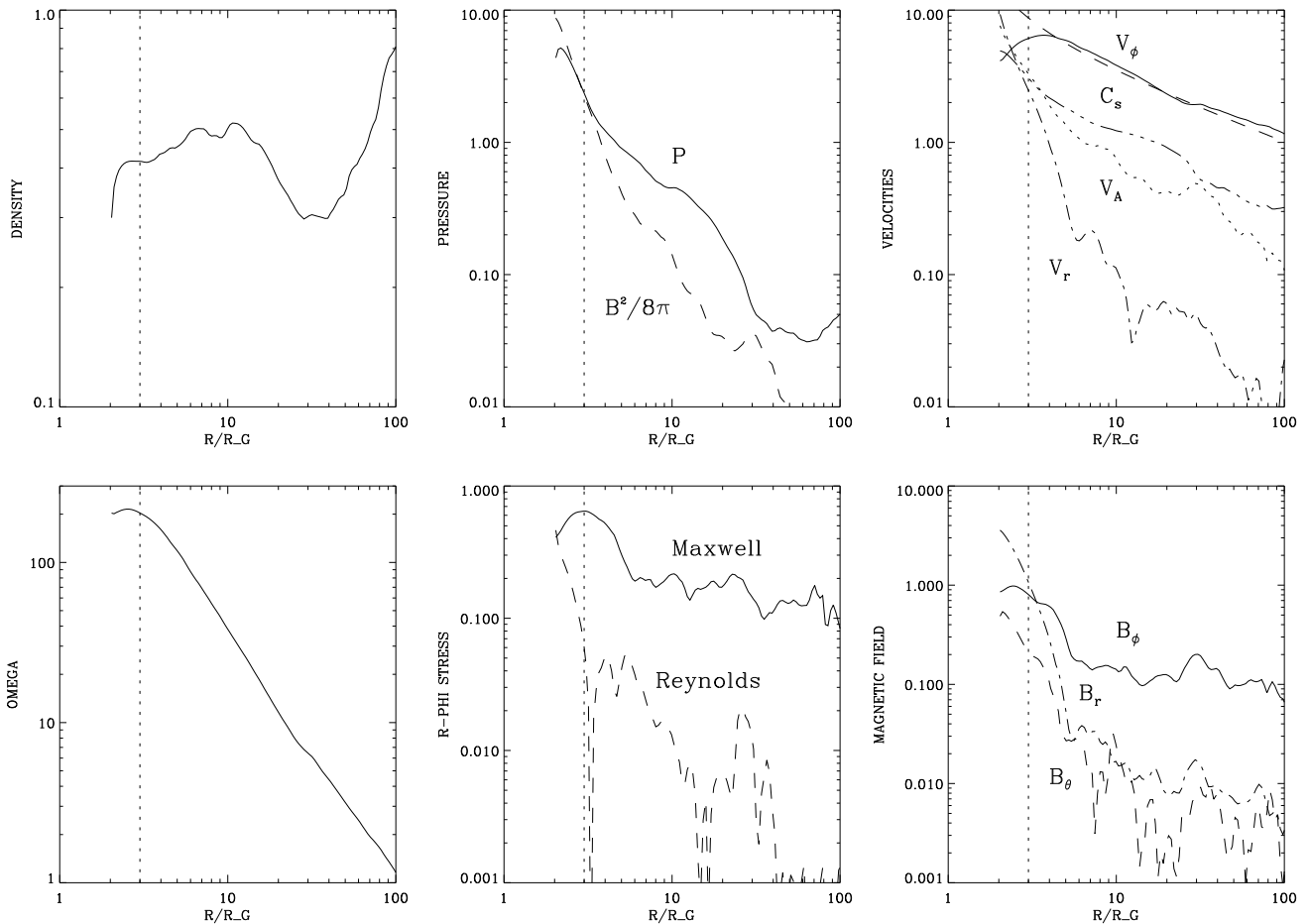


Figure 6. Radial scaling of some time-averaged quantities from Run F from orbits 3 through 5. The solution is averaged over angle between $\theta = 84$ and 96 degrees to construct each plot. The vertical dotted line in each plot shows the location of the last stable circular orbit. The dashed line in the plot of v_ϕ denotes Keplerian rotation at the equator. The Reynolds stress is calculated using equation 9, only its amplitude is shown.

SPB showed that in purely hydrodynamical flows driven by an anomalous shear stress, \dot{M}_{in} increases rapidly with radius. However, the inward mass flux is nearly exactly balanced by a large outward mass flux in the flow associated with convective eddies, so that the net mass accretion rate \dot{M}_{acc} defined in equation 8 is constant with radius. The magnitude of the accretion rate \dot{M}_{acc} is set by the properties of the flow at the inner boundary, and therefore is small compared to the mass inflow rate \dot{M}_{in} at large radii.

To compare how the mass fluxes vary with radius in the MHD flows, in Figure 7 we plot \dot{M}_{in} , \dot{M}_{out} , and \dot{M}_{acc} for Runs E and F, that is models with $\beta_o = 100$ and 200 respectively. In both cases, there is virtually no mass outflow within $10R_G$. Beyond $10R_G$, however, both the inward and outward mass fluxes increase rapidly, whereas their sum remains constant. By the outer regions of the flow, the mass inflow rate is two to four times the mass accretion rate. It is not possible to measure the radial dependence of the increase in the inward mass flux for these MHD models because of the limited dynamical range in radius.

4 DISCUSSION

The most important result of previous hydrodynamical simulations of non-radiative accretion flows is that although the inward mass flux associated with convective eddies is large, the net mass accretion rate is small and set by the physical conditions at the inner boundary. Although this result was not expected from standard self-similar solutions for ADAFs, analytic models which reproduce the results of the simulations have been developed with the ansatz that convection transports angular momentum inwards in axisymmetry (Narayan, Abramowicz, & Igumenshchev 2000; Quataert & Gruzinov 2000).

The mass accretion rates observed in the two-dimensional MHD models presented in this paper are consistent with the hydrodynamical simulations, that is \dot{M}_{acc} is again small compared to the expectations of a typical ADAF model. However, in the case of MHD models, turbulent eddies are not driven by convection but rather the MRI. In the MHD models there is no parameter that controls the magnitude of the shear stress. Instead, the magnitude of the Maxwell stress scaled to the magnetic pressure α_{mag} results self-consistently from the dynamics. Thus, it is impos-

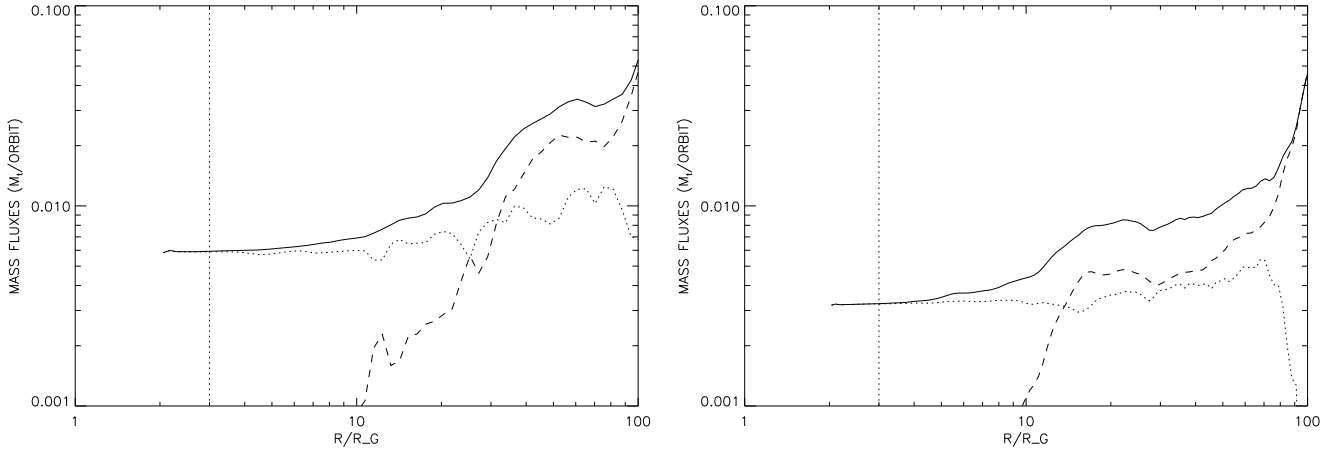


Figure 7. Radial scaling of the amplitude of the total mass inflow rate \dot{M}_{in} (solid line), total mass outflow rate \dot{M}_{out} (dashed line), and the net mass accretion rate \dot{M}_{acc} (dotted line) in Run E (left) and Run F (right). These fluxes are defined by equations 8, 10, and 11 in the text. The vertical dotted line in each plot shows the location of the last stable circular orbit.

sible to explore how this result varies with the amplitude of the shear stress, as is typical for hydrodynamical models. We find that the small accretion rates reported here are produced even when $\alpha_{\text{mag}} \approx 0.1 - 0.2$ (note that the Shakura-Sunyaev α parameter for these flows may be much different than α_{mag}). The amplitude of α_{mag} and the mass accretion rates reported here are consistent with those given by Hawley (2000) from fully three-dimensional simulations. There is growing observational support for small mass accretion rates around black holes at the centers of nearby early-type galaxies, or the galactic centre, (Di Matteo, Carilli, & Fabian 2000; Agol 2000; Quataert & Gruzinov 2000), which provides encouragement for further exploration of the dynamics reported here.

The large Alfvén speed that can arise in regions of low density and strong magnetic field makes these MHD models considerably more expensive to compute than pure hydrodynamical simulations. Thus, we are not able to explore the dynamics over as large a radial domain as used in SPB, even in axisymmetry, nor can we evolve them for as long. Moreover, because of the lack of dynamo action to amplify the poloidal field in axisymmetry, accretion in our models dies away after a few orbits of the outer torus. This makes our determination of the radial scaling of the time- and angle-averaged flow ambiguous, but our results are consistent with $v_r \propto r^{-1}$, and $\alpha_{\text{mag}} = \text{constant}$.

In axisymmetry, we find accretion does not always occur because of turbulent transport of angular momentum by the MRI. For sufficiently strong fields, global magnetic stresses associated with the radial component of the field can drive outward angular momentum transport and inward mass accretion. In this case, we find unbound winds are produced, as suggested by Blandford & Begelman (1999), but never observed in the hydrodynamical simulations of SPB. The mass flux carried in the outflow is small compared to the mass accretion rate (typically the ratio of the two is 0.1). Moreover, the fraction of outflowing material that is unbound is small, and it carries a small fraction of the total outward angular momentum flux. However, perhaps stronger fields, or disks threaded by a net vertical flux would result in more powerful

MHD winds. On the other hand, in 3D the nonaxisymmetric MRI may destroy the smooth poloidal field structure and therefore inhibit the production of winds.

By using the pseudo-potential of Paczyński & Wiita, our simulations reveal some interesting feature of the flow near the event horizon of a black hole. We find that infall begins at $r = 6R_G$, well beyond the radius of the last stable circular orbit. We interpret this due to the high pressure in a thick accretion flow. The radial infall becomes superAlfvénic at $r = 3R_G$. The geometry of the magnetic field is modified by the inflow, so that $B_R \sim B_\phi$. As a consequence the $r - \phi$ component of the magnetic stress is increased significantly in the inner regions. This stress is non-zero at the radius of the last stable circular orbit. All of these effects are consistent with the expectations of recent analytic theory (Krolik 1999; Gammie 2000)

Another evolutionary effect that is important in the inner regions of the flow is the increase of net magnetic flux through the inner boundary due to inward advection. Although we study tori with zero net magnetic flux, the inner regions (which carry one sign of vertical field) are always accreted first. The vertical field associated with these regions is amplified by geometric compression, so that the poloidal field can exceed the toroidal field near the inner boundary. As the outer regions of the torus (which carry the opposite sign of field) begin to accrete they can reduce the net flux through the inner boundary. Of course, this effect is strongly enhanced by axisymmetry. It is not clear how large are the spatial correlations in a dynamo amplified field in 3D. However, because of the large range in spatial and temporal scales, it is possible that a small patch in the outer regions of the disk containing one sign of vertical flux may produce similar behavior if it is accreted before the region containing the other sign of field.

We have focused on the time-averaged properties of the flow in our simulations in order to compare to the results of steady-state theory. However, there are a variety of interesting effects evident in the instantaneous properties of the flow. For example, Figure 8 is a snapshot of the radial profile of the density and $r - \phi$ component of the Maxwell

stress at $t = 2.35$ orbits in Run C, taken along the equator ($\theta = 90^\circ$). Extremely large fluctuations in the stress (more than an order of magnitude) are evident, each of which is associated with a large peak in the density. These peaks represent coherent blobs of matter which move inwards radially and accrete periodically. The profile of the stress indicates that the blobs are formed by radial fluctuations in the stress. In loose terms, this behavior is analogous to the secular instability discussed by Lightman & Eardley (1974), although the assumption of axisymmetry may enhance the effect in our simulations. Such effects may imply the mass accretion rate in an MHD flow will always be highly time-variable.

Finally, it is important to consider what are the limitations of this current study. Most importantly, we have studied only two-dimensional, axisymmetric models. This has several important consequences. Firstly, we eliminate any nonaxisymmetric modes of the MRI, and therefore limit the amplitude of the saturated state (and perhaps shear stress). Secondly, sustained dynamo action is not possible in axisymmetry; on long timescales the MHD turbulence and accretion eventually dies away in two-dimensional calculations. This can be dramatically demonstrated by a simulation which begins with the same field geometry as studied here (field loops parallel to the density contours), but with the direction of the field reversing on short radial scales. In this case, the field reconnects, and the turbulence and accretion die away as soon as the MRI goes nonlinear. The models studied here are similar to flows with a net vertical flux in the sense that only the inner regions of the torus (with one sign of field) accrete on the timescale we have studied. (As discussed above, this also has the effect of driving an accumulation of net flux through the inner boundary.) The importance of some of these effects can be gauged by direct comparison of our results to the fully 3D simulations of Hawley (2000).

In addition to being restricted to axisymmetry, our study is also limited by the numerical resolution that is required for practical calculations. Since accretion is produced by a physical instability in the flow that drives MHD turbulence, it is important to capture that turbulence over a large range of scales. It is clear that fully three-dimensional simulations of MHD non-radiative accretion flows at high resolution over a large radial domain are warranted, but will be challenging.

5 CONCLUSION

We have presented the results of a series of time-dependent numerical MHD simulations of the evolution of non-radiative accretion flows around a black hole. By confining this study to axisymmetry, we can extend the calculations over a larger radial domain than is possible in three-dimensions. However, since sustained dynamo action is not possible in axisymmetry, accretion in our simulations is transient, and dies away after a few orbits of the outer disk. Still, the large dynamic range in radius in our simulations means that this represents thousands of orbits of the inner regions of the disk; we have studied the quasi steady-state flow that is produced in the inner disk during this time.

There are a number of interesting similarities and differences in the MHD flows studied here compared to previous hydrodynamical models (SPB, IA99).

We find the net mass accretion rate is smaller than the mass inflow rate at larger radii. Over a large fraction of the accretion flow mass inflow is balanced by mass outflow associated with turbulent eddies. These eddies are driven by the MRI, rather than convection as in the hydrodynamical models. This can be dramatically demonstrated in our simulations by setting the resistive heating rate to zero; we find turbulence and accretion driven by the MRI continues in this case.

The two-dimensional time-averaged structure of the flow is very different than the hydrodynamical models. Contours of the density and pressure are nearly parallel, contours of the entropy and specific angular momentum are not aligned, and the rotational frequency is constant on cylinders. It may be that the two-dimensional structure emerging in these simulations is consistent with marginal stability to the generalized Høiland criterion in rotating, entropy-stratified, and weakly magnetized flows (Balbus 1995), although further theoretical work is required to confirm this.

The accretion flow is highly time-dependent. A snapshot of the flow shows that the amplitude of the Maxwell stress driving accretion, and the density of the flow can fluctuate by an order of magnitude on the local orbital timescale.

We find that accretion in these axisymmetric simulations proceeds both by turbulent flow driven by the MRI, and an ordered infall/outflow pattern driven by global stresses associated with an ordered poloidal field. The latter occur when the field is strong enough that the wavelength of the fastest growing mode of the MRI is longer than the scale height of the torus. However, in 3D the nonaxisymmetric MRI may make it more difficult to achieve the ordered infall/outflow pattern.

These simulations suggest that the enormous range in timescales between the inner and outer regions of an accretion disk introduces complex dynamical behavior if those regions are coupled through a magnetic field. Future three-dimensional simulations that span as large a radial domain as used here promise to reveal much about the nature of non-radiative accretion flows onto compact objects.

Acknowledgments: JS gratefully acknowledges financial support from the Institute of Astronomy, and from NSF grant AST-9528299 and NASA grant NAG54278.

APPENDIX A: ARTIFICIAL RESISTIVITY

In order to convert the magnetic energy dissipated in current sheets into thermal heating, we add an explicit artificial resistivity to the induction equation. The coefficient of artificial resistivity is given by

$$\eta = \frac{Q(\Delta x)^2}{\sqrt{\rho}} |\mathbf{J}| \quad (\text{A1})$$

where Δx is the grid spacing, and Q is a dimensionless constant. This form is similar to that adopted by Magara, Shibata, & Yokoyama (1997) in studies of reconnection in the solar corona. The numerical implementation of the artificial resistivity follows the technique outlined in Fleming, Stone, & Hawley (2000) for Ohmic dissipation, that is the resistive dissipation $\eta \mathbf{J}$ is treated as an effective electromotive force used in the constrained transport scheme to update the magnetic field components (Stone & Norman 1992b).

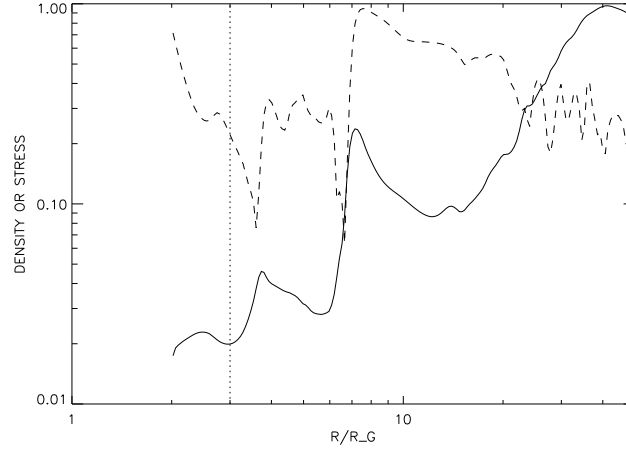


Figure 8. Instantaneous radial profile of the density (solid line) and $r-\phi$ component of the Maxwell stress (dashed line) at $t = 2.35$ orbits in Run C. The vertical dotted line shows the location of the last stable circular orbit.

The amplitude Q is specified by the requirement that the magnetic Reynolds number $Re_M = \Delta x V_A / \eta$, where $V_A = B / \sqrt{4\pi\rho}$ is the Alfvén velocity, be of order unity in current sheets in order for them to be spread out over a few zones. Substituting the form for η given above yields $Q = 1/\sqrt{4\pi}$ for $Re_M = 1$. We have run several simulations with different values of Q , keeping track of the evolution of the each component of the total energy in the flow. For $Q = 0$ in Run B we find the change in the total energy in the flow is 0.6% after 2.7 orbits of evolution. Using an artificial resistivity with $Q = 0.1$ this change is reduced to 0.08%, with most of the difference resulting from an increase in the total thermal energy. Thus, with an artificial resistivity, conservation of total energy is improved because energy losses due to numerical reconnection are reduced, and instead magnetic energy is converted directly to thermal energy in current sheets. An explicit artificial resistivity as introduced here could be important for any flow in which heating due to magnetic reconnection is important that is studied using a numerical algorithm that solves the internal (rather than total) energy equation.

REFERENCES

- Abramowicz, M.A., Chen, X., Kato, S., Lasota, J.-P., & Regev, O., 1995, *ApJ*, 438, L37
- Agol, E., 2000, preprint (astro-ph/0005051)
- Armitage, P., 1998, *ApJ*, 501, L189.
- Balbus, S.A., 1995, *ApJ*, 453, 380.
- Balbus, S.A., & Hawley, J.F., 1998, *Rev. Mod. Phys.*, 70, 1.
- Begelman, M.C., & Meier, D.L., 1982, *ApJ*, 253, 873
- Blandford, R.D., & Payne, D.G. 1982, *MNRAS*, 199, 883.
- Blandford, R.D., & Begelman, M.C., 1999, *MNRAS*, 303, L1.
- Brandenburg, A., Nordlund, A., Stein, R.F., & Torkelsson, U., 1985, *ApJ*, 446, 741
- Cabot, W., 1996, *ApJ*, 465, 874.
- Di Matteo, T., Carilli, C.L., & Fabian, A.C., 2000, preprint (astro-ph/0005516)
- Fleming, T.P., Stone, J.M., & Hawley, J.F., 2000, *ApJ*, 530, 464.
- Gammie, C.F., 2000, preprint (astro-ph/9906223)
- Hawley, J.F., & Balbus, S.A., 1992, *ApJ*, 400, 595.
- Hawley, J.F., Gammie, C.F., & Balbus, S.A., 1995, *ApJ*, 440, 742
- Hawley, J.F., Gammie, C.F., & Balbus, S.A., 1996, *ApJ*, 464, 690
- Hawley, J.F., 2000, *ApJ*, 528, 462.
- Igumenshchev, I.V., & Abramowicz, M.A. 1999, *MNRAS*, 303, 309 (IA99)
- Igumenshchev, I.V., & Abramowicz, M.A. 2000, preprint (astro-ph/0003397)
- Igumenshchev, I.V., & Abramowicz, M.A., & Narayan, R. 2000, preprint
- Kudoh, T., Matsumoto, R., & Shibata, K., 1998, *ApJ*, 508, 186.
- Krolik, J.H., 1999, *ApJ*, 515, 73.
- Lightman, A.P., & Eardley, D.M., 1974, *ApJ*, 187, L1.
- Matsumoto, R., 1999, in *Numerical Astrophysics*, eds. S. Miyama, K. Tomisaka, & T. Hanawa (Kluwer: Dordrecht), 195.
- Matsumoto, R., Uchida, Y., Hirose, S., Shibata, K., Hayashi, M.R., Ferrari, A., Bodo, G., & Norman, C., 1996, *ApJ*, 461, 115.
- Miller, K.A., & Stone, J.M., 2000, in preparation.
- Narayan, R., & Yi, I., 1994, *ApJ*, 428, L13
- Narayan, R., & Yi, I., 1995, *ApJ*, 444, 231
- Narayan, R., Igumenshchev, I.V., & Abramowicz, M.A., 1999, preprint (astro-ph/9912449)
- Quataert, E., & Gruzinov, A., 1999, preprint (astro-ph/9912440)
- Quataert, E., & Gruzinov, A., 2000, preprint (astro-ph/0004286)
- Quataert, E., & Chiang, E.I., 2000, preprint (astro-ph/0003368)
- Paczynski, B., & Wiita, J., 1980, *A&A*, 88, 23
- Papaloizou, J.C.B., & Pringle, J.E., 1984, 208, 721
- Shibata, K., & Uchida, Y., 1986, *PASJ*, 38, 631
- Stone, J.M., & Norman, M.L., 1992a, *ApJS*, 80, 753
- Stone, J.M., & Norman, M.L., 1992b, *ApJS*, 80, 791
- Stone, J.M., & Norman, M.L., 1994, *ApJ*, 433, 746
- Stone, J.M., Hawley, J.F., Gammie, C.F., & Balbus, S.A., 1996, *ApJ*, 463, 656
- Stone, J.M., & Balbus, S.A., 1996, *ApJ*, 464, 364
- Stone, J.M., Pringle, J.E., & Begelman, M.C., 1999, *MNRAS*, 310, 1002 (SPB).